

Determining case depth of low & medium carbon steels via Vicker's microhardness test

Robert Hawken

School of Engineering, University of the Sunshine Coast, 90 Sippy Downs Drive, Sippy Downs, 4558, QLD, Australia.

Abstract

Many machine elements such as gears and roller bearings involve constant wear and cyclic loading. The processes of surface hardening is employed in order to improve wear resistance of steels via carburizing. This report aims to test the case depth of case hardened and heat treated steels via a Vicker's Hardness test and propose a heat treatment plan. A diamond pyramid indentor was used to measure the Vicker's hardness value for 24 tests at 0.1mm increments with 100gf across two cross sections of processed steel. The lowest case depth was recorded in the 0.15%C heat treated steel (0.238mm) and the highest case depth was recorded in the 0.35% case hardened steel (2.01mm). These results are concurrent with the literature in relation to an increased microhardness in steels that are case hardened. At 1100° a proposed heat treatment plan determined that the 0.15% sample would take 3 minutes to case harden and 5 hours for the 0.35% sample. This data will be used to ensure case hardening of machine elements as they continue to be a crucial part of material fabrication, in order to improve wear resistance and plastic deformation to surface finishing.

1 Introduction

Surface hardness is the mechanical property of a materials resistance to scratching, indenting and plastic deformation. Microhardness testing of steels is completed using numerous technologies including corrosion, electrochemical and mechanical testing (Abdullrazzq 2016). The Brinell, Rockwell and Vicker's hardness tests are the most common mechanical hardness tests used in engineering practice. The Vicker's Hardness test is the most widely employed as it can be used on either soft or hardened steels and recorded in HV (Dossett & Totten 2013).

The process of carburizing is used to increase the surface hardness of steels, while the core of the material remains ductile. The penetration distance of carbon content that diffuses into the surface of steel is known as case depth, and this process is known as case hardening (Askeland 2011).

There are numerous applications in engineering practice which favours case hardening steels. Machine elements such as gears and roller bearings with continual contact and cyclic loading require very high surface hardening to increase durability and wear resistance, while remaining internally ductile for shock absorption (Dossett & Totten 2013). Due to the reliability required of gears and roller bearings, it is common practice for engineers to test the case hardening of samples before component manufacture (Vander 2004).

With respect to the previous foundations, it is hypothesised that case hardened steel will record significantly higher Vicker's hardness scores than heat treated samples with lower surface carbon content. These findings will be used to verify the current implementation of diffusion theory and case hardening in engineering material science.

2 Experimental Design

2.1 Methods and Materials

Two cross sectional steel samples were Vicker's microhardness tested by 3rd year mechanical engineering students at the University of the Sunshine Coast. Sample 1 was from a heat treated case ring made from 0.15wt% C low carbon steel while sample 2 was from a case hardened 0.35wt.% C medium carbon steel block.

A Struers DuraScan - 70 with overview camera was used to apply 24 indentations at 136° in 0.1mm increments with 100 gf (0.981N) force to each Bakelite mounted sample and recorded in Table A1.

The Durascan - 70 onboard software incorporated the average of diagonal indentation to calculate a Vicker's Hardness (HV) score and recorded in Table A1. The indentation angle and diagonal surface measurements can be seen in Figure 1.

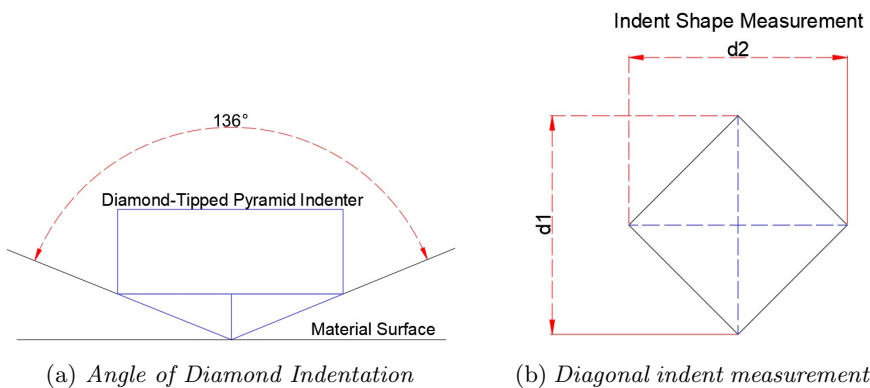


Figure. 1: Indentation angle and diagonal measurement of steel samples

2.2 Numerical Analysis

According to Dossett & Totten (V4,2013:p1018-1021), case depth for steels under 0.28%Cwt is determined as the corresponding surface depth for a Rockwell Hardness score of 50. Interpolation in MATLAB from the hardness test conversion chart displayed in Dossett & Totten (2013), arises a Vicker's Hardness score of 513. A Rockwell hardness value of 40 is used for steels with carbon content 0.33%-0.42%Cwt (Dossett & Totten 2013). MATLAB interpolation arises a HV value of 402. These HV values are used to Interpolate and graphically identify the corresponding case depth (Figure 2).

3 Results and Discussion

3.1 Analysis of Case depth of Steel samples

After numerical and graphical analysis and reference to Dossett & Totten (V4,2013:p1018-1021), the effective case depth of heat treated 0.15%Cwt is 0.238mm and case hardened 0.35%Cwt is 2.01mm (Figure 2). Case depth was estimated graphically and interpolated with MATLAB to return a more accurate estimation. The process of carburizing has shown that steels with a case hardened layer report higher HV values (Abdullrazzq 2016) and therefore remain more resistant to surface deformation (Callister 2018).

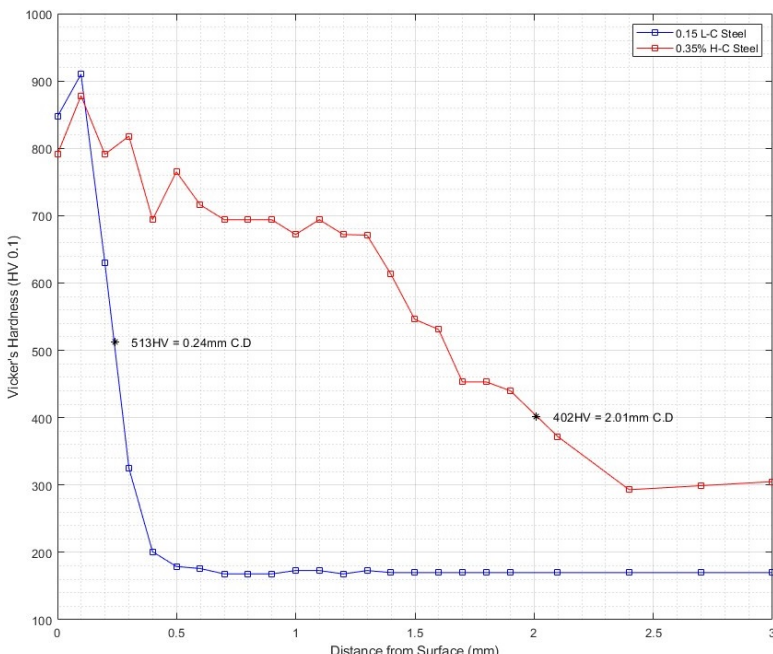


Figure. 2: Vicker's Hardness scores measured from material surface for 0.15% and 0.35% Carbon steel with interpolated case depth indication.

3.2 Analysis and Understanding of Photographic evidence

The HV score on the 0.15%C sample resulted in the instantaneous highest recorded result of 910 HV (Figure 3a). The following indentation tests recorded a reduction in hardness to 630 and 325 with 0.299mm into the surface. At the same 20x objective lens, the increase in indentation at T7 can be seen in Figure 3 b).

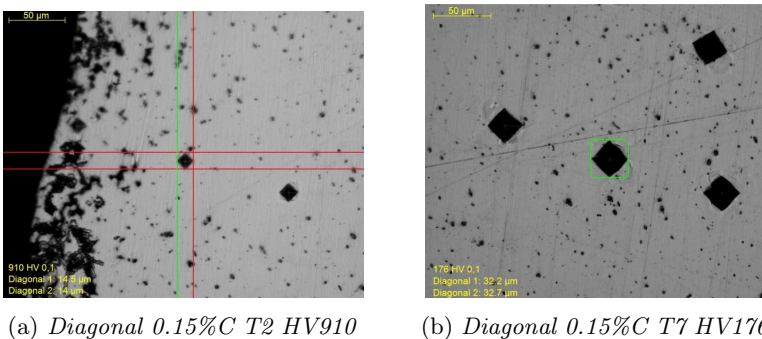


Figure. 3: Indentation of 0.15%C steel at initial and final values of HV

Conversely, Figure 4 shows the indentations of 0.35% steel at Test 2 and Test 23. Even though test 2 scored a lower HV of 878 compared to test 2 of 0.15% the indentation remained minimal in comparison. After 23 tests the HV score of 299 was recorded and remained 1.7 times higher than in Figure 3b). Along with the reduction in dark deposits of the sample in Figure 3, these photographs depict the increase in diagonal measurements and reduced case depth in 0.15% sample.

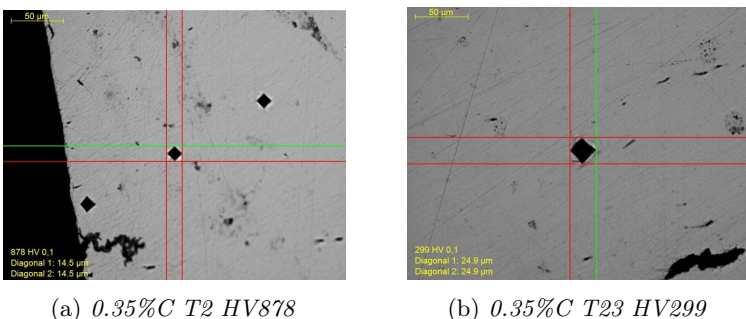


Figure. 4: Indentation of 0.35%C steel at initial and final values of HV

During the phase diagrams of $Fe + Fe_3C$, the carbon content is reduced out of the Eutectoid region $\approx 4.3\text{wt\%}C$ until it reaches the Eutectic valley $\approx 0.76\text{wt\%}C$ (Figure 5). Once the steel is under 0.76% carbon, then further treatments can be applied to reduce carbon content (Abdullrazzq 2016). As the overall carbon concentration reduces, the outer layers of the steel become easier to deface. The outer layer of the material is subjected to carbon diffusion to improve external wear resistance. In order to improve the hardness of these steels, a layer of carbon is diffused, known as carburizing (Callister 2018). Thus the process of case hardening is employed to increase surface hardness to a specific case depth (Abdullrazzq 2016).

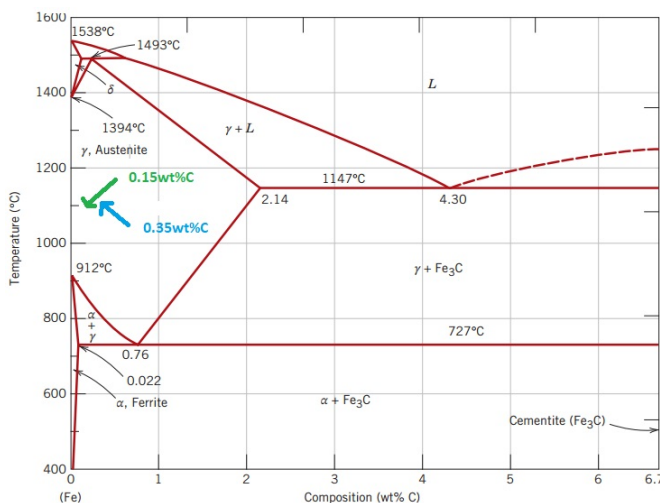


Figure. 5: $Fe + Fe_3C$ Phase Diagram with Austenite 1100° case hardening temperature indicated (Section 3.3)(Callister 2018)

With the known carbon concentrations and using industry standards and low and medium carbon steels, it is possible to design a heat treatment plan for these samples.

3.3 Heat treatment plan for determined case depths

After determination of case depth for each sample (Figure 2), it is possible to propose a heat treatment plan for interstitial carbon diffusion.

3.3.1 Heat Treatment Plan for 0.15% Low Carbon Steel

Based on appropriate carbon percentages for low carbon steel and interpolation of erf(z) scores, the following heat treatment plan could be followed to obtain 0.15% carbon case hardening at a case depth of 0.24 mm at both 1100° & 900° (Callister 2018). (Equation 1).

$$\frac{C_{x,t} - C_o}{C_s - C_o} = 1 - erf\left(\frac{x}{2\sqrt{Dt}}\right)$$

Equation 1: Solution to Fick's second order partial differential equation (EQ.1)

$$T = 1100^\circ \text{ } C_0 = 0.15\%, \text{ } C_x = 0.45\%, \text{ } C_s = 1.2\%, \text{ } D = 5.3 \cdot 10^{-11}$$

$$0.7143 = 0.755 \left(\frac{16.486}{\sqrt{t}} \right)$$

Time \approx 3 minutes @ 1100°

$$T = 900^\circ \text{ } C_0 = 0.15\%, \text{ } C_x = 0.45\%, \text{ } C_s = 1.2\%, \text{ } D = 5.9 \cdot 10^{-12}$$

$$0.7143 = 0.755 \left(\frac{49.403}{\sqrt{t}} \right)$$

Time \approx 45 minutes @ 900°

It can be seen that for 0.15% low carbon steel, that there is a 15x increase in diffusion time by performing the process at 900° when compared to 1100°. Figure 6 indicates the carbon diffusion rate with respect to temperature (Dossett & Totten 2013). The change in diffusion rate due to temperature is evident due to the nature of the curve (Figure 6).

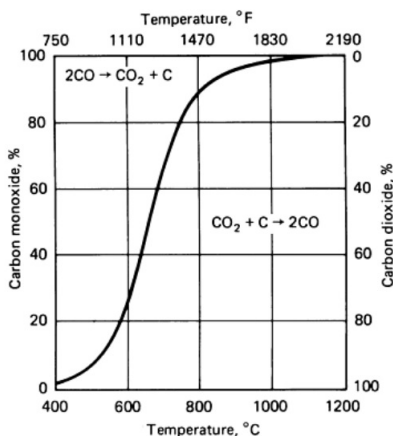


Figure. 7: Carbon diffusivity into steel occurs highest over 1000° (Dossett & Totten 2013)

3.3.2 Heat Treatment Plan for 0.35% Medium Carbon Steel

Based on appropriate carbon percentages for low carbon steel and interpolation of erf(z) scores, the following heat treatment plan could be followed to obtain 0.35% carbon case hardening at a case depth of 2.01 mm at both 1100° & 900° (Callister 2018). (Equation 1).

$$T = 1100^\circ C_0 = 0.35\%, C_x = 0.90\%, C_s = 1.6\%, D = 5.3 \cdot 10^{-11}$$

$$0.56 = 0.5461 \left(\frac{138.05}{\sqrt{t}} \right)$$

$$\text{Time} \approx 5 \text{ hours} @ 1100^\circ$$

$$T = 900^\circ C_0 = 0.35\%, C_x = 0.90\%, C_s = 1.6\%, D = 5.9 \cdot 10^{-12}$$

$$0.56 = 0.5461 \left(\frac{138.05}{\sqrt{t}} \right)$$

$$\text{Time} \approx 45 \text{ hours 12 minutes} @ 900^\circ$$

It can be seen that for 0.35% low carbon steel, that there is a 9x increase in diffusion time by performing the process at 900° when compared to 1100°. Figure 7 indicates the carbon case depth with respect to temperature (Dossett & Totten 2013). The increase in carburizing temperature with an increase in case depth, further verifies the results of this heat treatment plan. As 1100° was used, this would further increase carburizing times and would result in the 'blue' line intersecting the temperature gradient at 5 hours, as depicted in Figure 7.

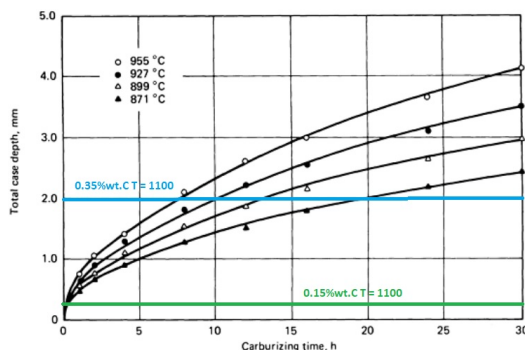


Figure. 8: Depiction of case hardening time and case depth. [Note this heat treatment plan $T = 1100^\circ$ will increase times displayed and verify the results] (Dossett & Totten 2013).

4 Conclusion

After analysis of calculations and experimental findings, it has been concluded that this experiment does verify material properties expected by 0.15% and 0.35% case hardened materials. The following conclusions were made;

1. The 0.15% sample recorded the highest hardness of HV 910 and lowest HV 176 compared to the 0.35% sample of HV 878 and HV 299.
2. However, the 0.35% sample recorded higher sustained HV values due to the thicker case depth (2mm) while the 0.15% sample had a drastic drop off after 3 tests due to the thinner case depth (0.24mm).
3. At the same carbon concentrations, for the 0.15% LC sample, it would take ≈ 3 minutes to case harden (0.24mm) at 1100° and 45 minutes at 900°.
4. At the same carbon concentrations, for the 0.35% MC sample, it would take ≈ 5 hours to case harden (2mm) at 1100° and 45 hours, 12 minutes at 900°.
5. Diffusion time is exponentially temperature dependent due to the nature of Fick's second order partial differential equations. (Equation 1).

These calculations are required in industry in order to recreate materials based off tested hardness values. These findings are used to verify the current implementation of diffusion theory and case hardening in engineering material science.

4.1 Error and Recommendations

The primary recommendation would involve the improved surface cleaning of the samples. Visible finger prints were noted during sampling and removal would have improved picture quality.

It is recommended for future studies to obtain different metals and alloys to broaden the array of tested materials. Due to the increased industry usage of stainless steels, it would be interesting to measure the surface hardness of these alloys.

References

1. Abdulrazzaq, M. (2016). Investigation: The Mechanical Properties of Carburized Low Carbon Steel. International Journal of Engineering Research and Application, 6(9), pp.59-65. ISSN : 2248-9622.
2. Askeland, D.R., Fulay, P.P. and Wright, W.J. (2011). The science and engineering of materials. Stamford, Ct: Cengage Learning.
3. Callister, W.D. (2018). Materials science and engineering : an introduction 10E. Hoboken, New Jersey: John Wiley Sons.
4. Dossett, J.L., Totten, G.E. and ASM International. Handbook Committee (2013). ASM handbook. Volume 4, Heat treating. Materials Park: ASM International.
5. Vander, G.F. and Asm International. Handbook Committee (2004). ASM Handbook, Volume 9. Metallography and Microstructures. Materials Park: ASM International.

Fracture mechanics of engineering materials via Charpy impact testing

Robert Hawken

School of Engineering, University of the Sunshine Coast, 90
Sippy Downs Drive, Sippy Downs, 4558, QLD, Australia.

Abstract

Impurities and variations in treatment processes during metal, alloy and plastic manufacturing changes the architecture of materials outside of the published and agreed values. The mechanical properties of steels, alloys and plastics can be effected by changes in temperature.

ASTM A370 Charpy Impact testing was conducted on Low Carbon Steel, Tool Steel, Aluminium and α -Brass samples. ASTM D256 standard was conducted on Polyvinyl Chloride samples. These samples were at ambient room temperature and new samples were submerged in Liquid Nitrogen $LN_2 \approx 77K$.

Low Carbon Steel and Tool Steel had an energy absorption reduction of 72.7% and 82.8% respectively post impact between ambient and LN_2 tests. Aluminium and α -Brass recorded no significant difference in energy absorption between ambient and LN_2 temperatures. These results suggest that, ductile to brittle transformations (DTBT) occur in BCC materials with a reduction in temperature at 77K.

This is consistent with the literature and is due to the nature of the body centered cubic crystal structure of Low Carbon Steels, Tool Steels and similar to polymers. Face centered cubic materials such as Aluminium and α -Brass do not undergo DTBT due to a reduction in temperature.

1 Introduction

Verification of material toughness can be determined by a variety of mechanical tests. The Charpy impact test is most commonly used to determine a materials fracture toughness via energy absorption pre and post impact (Mouritz 2012). This test can be used to infer a materials energy absorption and fracture toughness (KI_c) (Callister 2018). Aerospace applications factor in the likely hood of impact and the consequences of such at a variety of temperatures. With respect to the newly launched James Web Space Telescope (JWST), it is prone to minor debris strikes and operates in temperatures $\approx 77K$ in orbit on the far side of the moon (Figure 1, NASA Goddard 2022).

To reduce the consequences of impact, the outer layer of the telescopes sun shield is coated in Aluminium, due to the crystal structure of a face centered cubic (FCC) material (NASA Goddard 2022). Aluminium does not undergo a Ductile to Brittle Transformation (DTBT) upon impact due to the crystal structure and slip system differences between steels (Askeland, Fulay & Wright 2011 and Dennies 2020). Most steels are body centred cubic crystal structures (BCC) as they undergo a DTBT with impact at colder temperatures. Even though steels have a much higher Young's Modulus than aluminium (200 GPA vs 70 GPA), the materials crystal structure is more important at such low temperatures (Mouritz 2012).

As the JWST operates in temperatures close to the liquid point of Nitrogen $\approx 77K$, it is suitable to use materials at a similar temperature in a Charpy impact test for verification of the aforementioned material properties. It is hypothesised that with a reduction in temperature the BCC crystal structure materials will undergo a DTBT and the materials that are FCC will not. These findings will coincide with the reasoning for the FCC material choice observed on the outer layers of the JWST sunshade.



Figure. 1: Infographic depicting temperature change of Telescope and Aluminium outer coatings of the James Web Space Telescope. (*Image courtesy of NASA*)

2 Experimental Design

Charpy impact testing was completed at the University of the Sunshine Coast. ASTM A370 standard samples of Low Carbon Steel, Tool Steel, Aluminium, α -Brass and ASTM D256 standard for Poly-Vinyl Chloride (PVC) were used. One impact test was completed on each of the five engineering materials at ambient room temperature $\approx 297K$ and on five more samples, stored in Liquid Nitrogen (LN_2) at ≈ 77 Kelvin.

A 4kg Impact hammer was mounted to a shaft with radius 345mm and a 140 degree initial angle was used. (Figure 2 a) After manual release, the final Impact hammer angle measured by eyesight and fixed protractor after each

test (Table 1, Appendix 1).

An example of the Impact hammer final angle after sample fracture can be seen in Figure 2 (b).

Potential Energy of the Impact Hammer pre and post impact was calculated using Microsoft Excel 365.

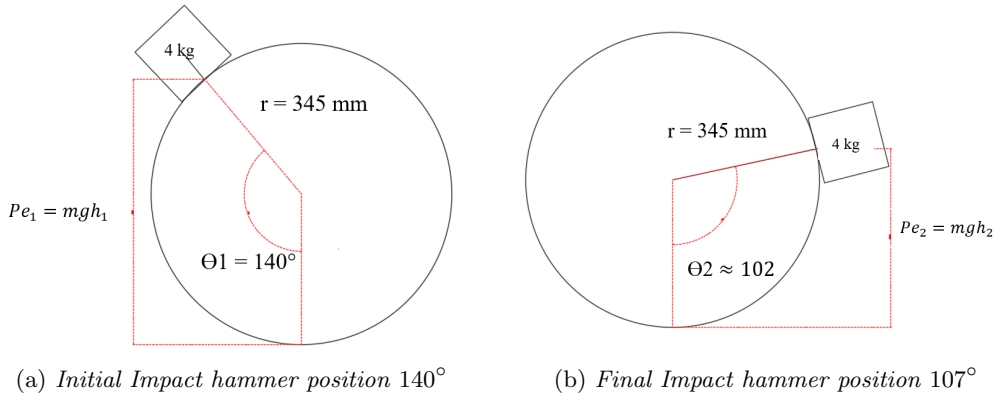


Figure. 2: Angular motion of Impact hammer before and after Low Carbon Steel test at ambient temperature

The experimental design of the Impact zone used in the Charpy Impact test can be seen in Figure 3. If the material fractured on impact, the follow through angle was measured to estimate energy transfer (Figure 3). If the material did not fully fracture, the resulting rebound angle was recorded (Table A1, A2).

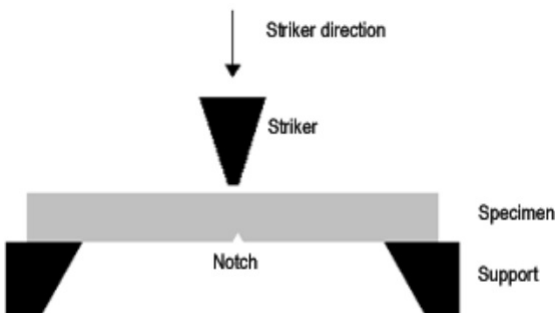


Figure. 3: Striker and support set up at material impact.

3 Results and Discussion

The initial and final Impact hammer angle and energy absorption results can be seen in Table A1 and Figure 4 respectively.

3.1 Comparison between metals, alloys and PVC post impact

Figure 4 shows the Potential energy absorption between ambient and LN_2 temperatures. The values for energy absorption were calculated via comparing the initial and final angles of the impact hammer, pre and post striking each material. The potential energy changes were calculated using equation (1).

$$E = mgr[\cos(\theta_2) - \cos(\theta_1)] \quad (1)$$

As mass, acceleration due to gravity and radius of the hammer remain constant, only the cosine of the resultant angle needs to be considered (Equation 1, Table A1).

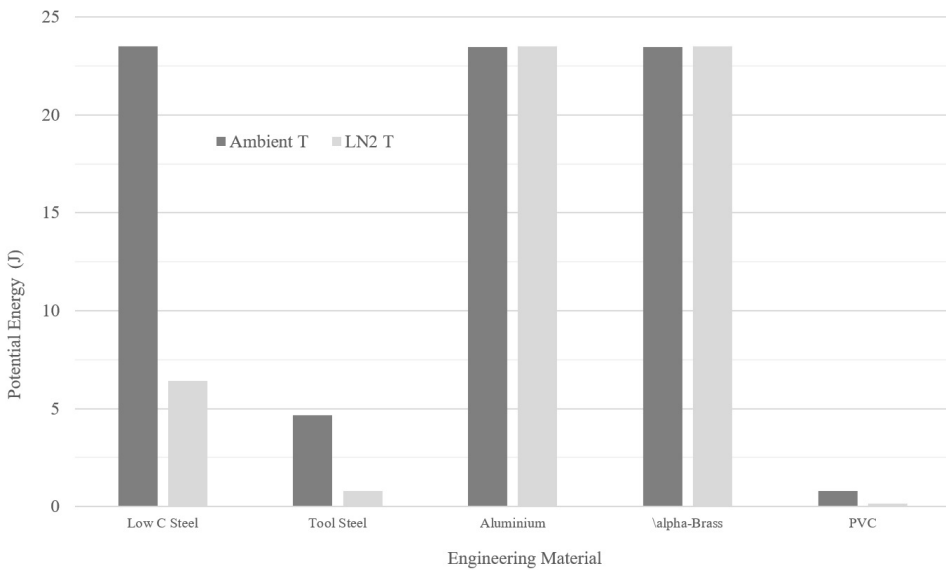


Figure. 4: Absorbed Potential Energy between Ambient and LN_2 material testing.

It is seen that a similar energy absorption was recorded in Low Carbon Steel, Aluminium and α -Brass at Ambient temperature $\approx 23.5\text{J}$ (Figure 4).

These materials all plastically deformed on impact and did not fully fracture from visual inspection. Tool Steel observed the lowest energy absorption of

any metal at ambient temperature with 4.6 J absorbed and therefore sustained a full fracture.

PVC absorbed very little potential energy at impact and also sustained a full fracture for both temperature tests (Figure 4). The graphical change is seen between the two samples for each testing temperature, however Table 1 displays further numerical analysis of the relative difference between each sample at the different temperatures.

3.2 Investigation of energy change between temperatures

It can be seen that Low Carbon Steel (72.8%) and Tool Steel (82.8%) had the highest relative energy change between the two tests when compared with the two other metallic materials (Table 1). PVC also recorded a relative energy change of over 80% (Table 1).

Aluminium and α -Brass both returned a negligible energy loss as nearly all energy was absorbed in the process of plastically deforming the materials.

Table 1: Change in Energy Absorption from LN_2 compared to Ambient Temperature

Material	Crystal Structure	Total Energy Change (J)	Relative Energy Change (%)
Low Carbon Steel	BCC	17.1	72.7
Tool Steel	BCC	3.9	82.8
Aluminium	FCC	≈ 0	≈ 0
α – Brass	FCC	≈ 0	≈ 0
PVC	Amorphous	0.6	80.8

Note: Full recorded data is found in Appendix A

3.3 Investigation of DTBT and Fracture Toughness of Metals

It can be seen there is a significant difference in energy absorption between the two steel samples and PVC. These findings are concurrent with published literature of BCC DTBT (Dennies 2020 and Mouritz 2012)).

With reference to Figure 5, the Mouritz (2011) graphic depicts the change of fracture toughness with the change in temperature. The reduction in temperature can be seen to reduce fracture toughness of the BCC metals, but not the FCC metals. The fracture toughness stated by Low carbon steel is

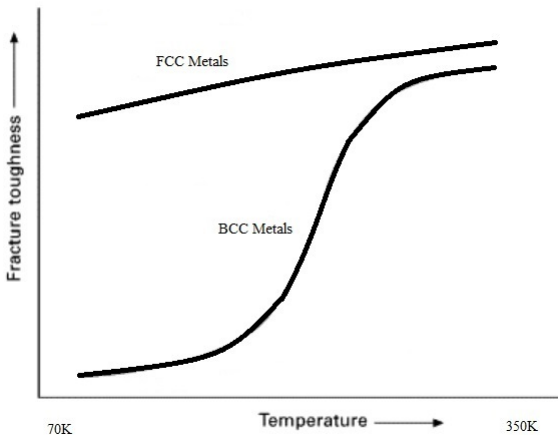


Figure. 5: Ductile to Brittle fracture trends of metal crystal structure types

$50MPa\sqrt{m}$ and Tool steel of $25MPa\sqrt{m}$ at ambient temperature (Callister 2018 and Dennies 2020). This reduces significantly when moving towards 70K (Figure 5). The fracture toughness of Aluminium $40MPa\sqrt{m}$ and α -Brass $40 - 51MPa\sqrt{m}$ does not significantly change with a reduction in temperature due to the dislocation nature of FCC crystal structure metals (Callister 2018 and Azom.com).

Fracture toughness was not directly measured due to the inability to measure crack length via Scanning Electron Microscope (SEM). However fracture toughness can be inferred during its proportional relationship to energy absorption (Mouritz 2011). The charpy impact test was able to accurately predict the DTBT region for the BCC metals as expected (Figure 5).

3.4 Investigation of DTBT and Fracture Toughness of Polymers

Polymers with low tensile elongations such as PVC are known as brittle polymers and ASM Volume 11 (Dennies 2020) indicates that PVC will fracture easier at lower temperatures as the nature of an Amorphous polymer. Table A2 indicates 1° change after impact at 77K, resulting in an 80.8% reduction in energy absorption. With an ambient fracture toughness of $2 - 4MPa\sqrt{m}$ this represents the under 1 J of energy absorbed at room temperature. (Table 1, A1).

Polymer failure at low temperatures can be seen in the Challenger Space Shuttle disaster. In 1986, a total loss of spacecraft and astronauts occurred due to a polymer DTBT .The Overnight temperature reduced from 24° to -13° caused a DTBT like rupture of a polymer O-ring on a Solid Rocket Booster upon loading (Mouritz 2011 and Callister 2018). The results from this experiment are in line with example of polymer DTBT occurring, hence the 1° angular change at 77K.

4 Conclusion

After analysis of calculations and experimental findings, it has been concluded that this experiment does verify material properties expected by FCC and BCC metals. The amorphous PVC also conducted a DTBT as expected. It was hypothesised that the BCC crystal structure materials will undergo a DTBT and the materials that are BCC will not, with a reduction in temperature. These findings do coincide with the reasoning for the FCC material choice observed on the outer layers of the JWST sunshade and change in materials for SRB O-rings.

4.1 Error and Recommendations

With reference to Section 3.1 and 3.2, as there was one trial for each test, minimal measurement or experimental error could be obtained. It is recommended to use a digital measurement of angle instead of using an analogue mounted protractor. Even though the impact hammer follows the path of the recording needle, a digital sensor would increase accuracy.

It is recommended for future studies to obtain different metals and alloys to broaden the array of tested materials. As Austenitic steels are of BCC crystal structure, it is recommended to test this material as theoretically it would have the same energy absorption as aluminium and α -Brass and not undertaken a DTBT (Vander 2004). Due to the increased industry usage of Carbon and Glass, Fibre Reinforced Polymers (CFRP) and GFRP, it is recommended to incorporate different polymers for Impact testing as well.

References

1. Askeland, D.R., Fulay, P.P. and Wright, W.J. (2011). The science and engineering of materials. Stamford, Ct: Cengage Learning.
2. Callister, W.D. (2018). Materials science and engineering : an introduction 10E. Hoboken, New Jersey: John Wiley Sons.
3. Dennies, D.P. (2020). ASM Handbook, Volume 11. Failure Analysis and Prevention. Materials Park: ASM International.
4. (NASA, Goddard) (2022). Sunshield Coatings Webb/NASA. [online] Available at: <https://webb.nasa.gov/content/about/innovations/coating.html>.
5. Mouritz, A.P. (2012). Introduction to aerospace materials. Reston, Va: American Institute Of Aeronautics And Astronautics ; Cambridge, Uk.

6. Properties: Copper Alloys - Brasses. AZoM.com. [online] Available at: <https://www.azom.com/properties.aspx?ArticleID=62>.
7. Vander, G.F. (2004). ASM Handbook, Volume 9.Metallography and Microstructures. Materials Park: ASM International.

Appendix A

Table A1: Izod Impact Results with ambient 297 K T°

Material	θ_u	θ_f	$\Delta\theta$	$E_{absorbed}$
Low Carbon Steel	140	14	126	23.51
Tool Steel	140	115	25	4.65
Aluminium	140	15	125	23.45
α - Brass	140	14	126	23.45
PVC	140	135	5	0.8

Table A2: Izod Impact Results with LN_2 77K T°

Material	θ_u	θ_f	$\Delta\theta$	$E_{absorbed}$
Low Carbon Steel	140	107	33	6.41
Tool Steel	140	135	5	0.8
Aluminium	140	14	126	23.51
α - Brass	140	14	126	23.51
PVC	140	139	1	0.15

Additional Information: Further information of the experimental design can be obtained by contacting the University of the Sunshine Coast, School of Engineering, MEC - 301, Materials Technology Impact Test Laboratory Manual, 90 Sippy Downs Drive, Sippy Downs QLD 4556.

Determining heat flow of engineering metals in steady state conduction

Robert Hawken

School of Engineering, University of the Sunshine Coast.

1 Introduction

The nature of metallic atomic bonding varies greatly between polymers and ceramics due to the 'sea of electrons' available for electrical and thermal conduction in metals. The amount of available electrons for either electrical or thermal conduction is determined by the arrangement of valence electrons in the most outer electron shell (Callister 2018).

Thermal conduction in metals is determined by the process of electron collisions, by passing high vibrational energy along a temperature gradient and which is denoted as k (Askeland and Wright 2016). The efficiency of electron motion is determined by the arrangement of electrons, impurities and material properties between alloys (Callister 2018).

Due to the nature of steady state thermal conduction appearing as a wave, it is possible to measure the heat flow through materials between two known points. Fourier's law of heat conduction is used to describe the relationships between each parameter (Cengel and Ghajar 2015). The heat flow rate is directly proportional to the thermal conductivity value, cross sectional area and temperature difference and inversely proportional to the distance the heat flow travels (Cengel and Ghajar 2015).

Understanding thermal conductivity is paramount for many engineering applications as the rate of heat flow through a material can be measured to manage thermal safety and operational requirements (Askeland and Wright 2016).

With respect to the previous foundations of steady heat conduction, it is hypothesised that materials with higher thermal conductivity values will have decreased time when measuring temperature change over a known distance. These findings will be used to verify the current implementation of thermal conduction management in engineering heat transfer and material science.

1.1 Governing Equations

The primary equations used for this experiment is Fourier's Law of Heat Conduction. This formula is derived from a partial differential equation and can be used to find the rate of heat flow in Joules per second, with known thermal conductivity, material cross sectional area, change in temperature and known distance of heat transfer.

$$\frac{\Delta Q}{\Delta t} = \frac{k \cdot A \cdot \Delta T}{0.030} \quad (1)$$

The heat pulse can be calculated by the distance over the time taken for thermal conduction to occur.

$$\vec{v}(\frac{m}{s}) = \frac{\Delta x(m)}{\Delta t(s)} \quad (2)$$

2 Experimental Design

2.1 Conduction Race Methods and Materials

A TD-8513 thermal conduction kit was used with material samples of 6063-T5 Aluminium ($90 \times 12 \times 4$ mm), 304 Stainless Steel ($90 \times 12 \times 4$ mm) and two 360-alloy Brass samples with different widths ($90 \times 12 \times 4$ mm & $90 \times 7 \times 4$ mm). In Heat mode, the TD-8513 device was subjected to 5V DC power supply with a temperature sampling rate of 5Hz for 5 minutes. Insulating foam was placed over the material samples to reduce convection (Figure 1). The temperature and time at each thermistor was recorded with the provided software and processed in MATLAB (Figures 2, 3 & 4).

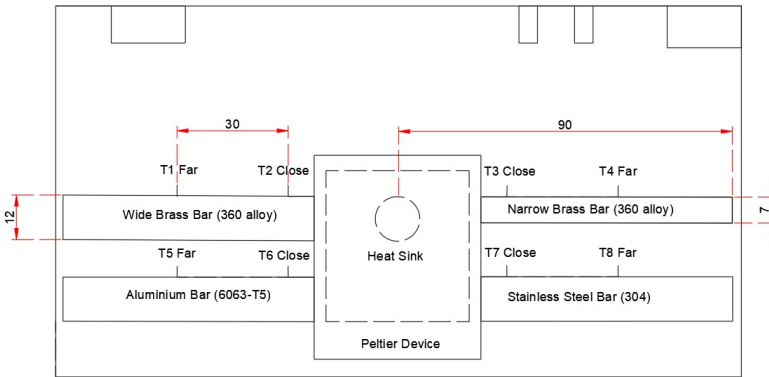


Figure. 1: Peltier Device TD-8513 with Thermistors placed 30mm apart

2.2 Heat Pulse Methods

Following the same power and initial procedure in section 2.1, the temperature sampling rate was set to 2Hz once the samples returned to room temperature. Once the temperature of T2 reached 40° the Peltier device was changed from Heat mode to Cool mode each 30 seconds for 5 minutes. Temperature difference between close and far thermistors was recorded and presented in Figure 4 & 5.

2.3 Numerical Analysis

PASCO manufactures provide thermal conductivity values for the engineering materials based on each specific alloy. Graphical illustrations of collected data and gradient of tangent lines denoting rate of temperature change was completed using MATLAB 2022Ra edition. Heat Flow rate and Heat Pulse for each engineering material 30mm apart was calculated using Microsoft Excel 365.

3 Results and Discussion

3.1 Conduction Race (*Following methods from section 2.1*)

The temperature recordings from the 'far' thermistors of each engineering material is displayed in Figure 2. The most efficient heat conductor is Aluminium at Thermistor position T5, reaching 40 degrees after 5 minutes.

In the first 50 seconds, the gradient of temperature change of aluminium was 0.17, this is due to the relatively high thermal conductivity rating of Aluminium 6063-T5 is $150\left(\frac{W}{m \cdot K}\right)$ (Bluesea 2019).

The least efficient heat conductor is Stainless Steel at Thermistor position T8. In the first 50 seconds, the gradient of the temperature change was 0.003. This difference results in Aluminium increasing temperature at 55 fold faster than Stainless Steel (Figure 2) over the 30mm span.

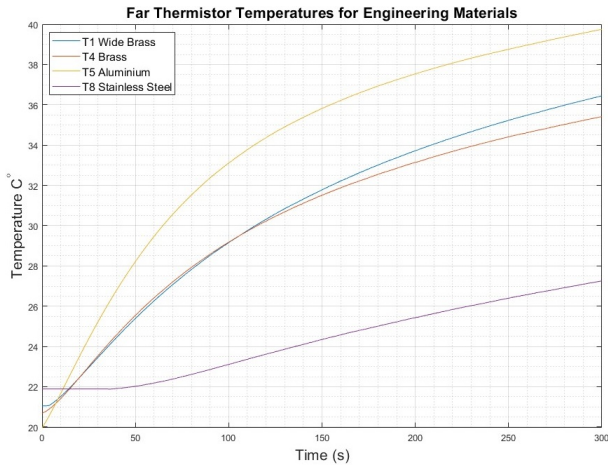


Figure. 2: Temperatures from Far Thermistors for Engineering materials

Minimal gradient differences were observed between Brass samples. The 12mm wide sample experienced the higher overall temperature, however less than one degree Celsius difference after 5 minutes (Figure 2). Following the properties of Fourier's Law of Heat conduction (Eq. 1), it is evident that heat flow is time and distance dependent (Chung, 2001). In the Wide Brass sample, it took 3.2 seconds for the temperature in the far thermistor (T2) to register temperature change (Figure 3). Equation 2 results in a Wide Brass heat pulse of $9.4(\frac{mm}{s})$.

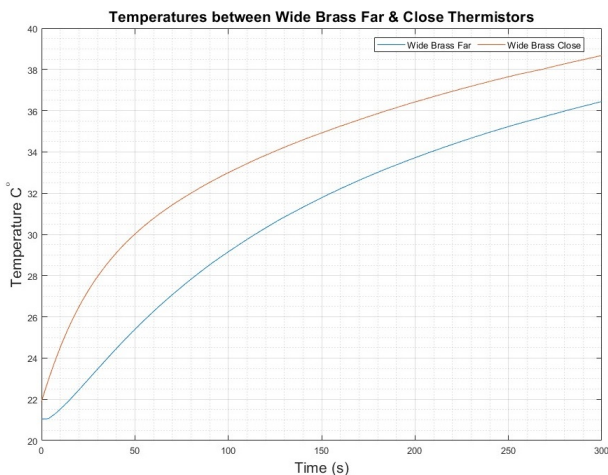


Figure. 3: Wide Brass Temperatures from Close and Far Thermistors

To further understand the relationships of material properties, thermal conductivity and heat flow rate, it is important to compare the temperature change between thermistors within the same sample (Figure 4) (Chung, 2001).

Stainless Steel observed the highest overall temperature difference $\approx 9^\circ$, which in fact had properties similar to a thermal insulator (Figure 4) (Cengel and Ghajar 2015). Thermal energy takes longer to arrive at the far thermistor due to the 30mm distance (Ozis and Tzou, 1994). Aluminium had the smallest temperature difference over the 30mm distance $\approx 0.9^\circ$ and therefore was the most efficient thermal conductor (Figure 4). This correlation is evident following the material property tables (Table 1) [AZoM (2019), Brass 360 (2022), Eng Toolbox (2019), Pasco (2022)].

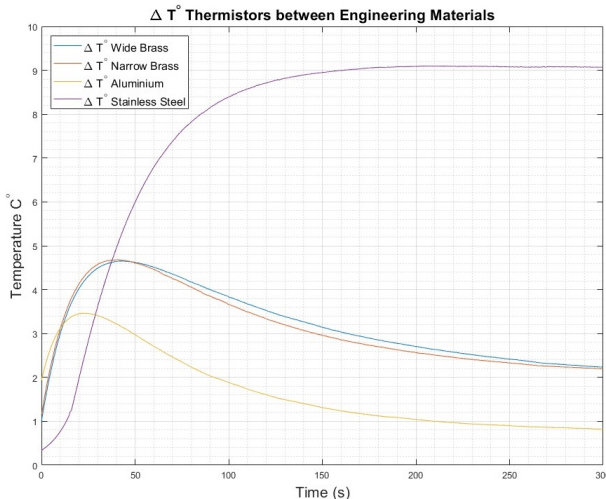


Figure. 4: Δ Temperature of Close and Far Thermistors for each Metal

Table 1 indicates that Aluminium is the most pure substance with 97.5% whereas both brass and Stainless Steel samples are $\approx 60\%$ alloy. This verifies the high thermal conductivity of Aluminium, however it has the lowest heat flow rate of 0.28 (J/s) (Equation 1). These values indicate that Aluminium does conduct heat faster, however it is not able to transfer as much total heat transfer compared to the other materials (Ozis and Tzou, 1994).

Table 1: Material properties & Heat flow rate \dot{Q}

Property	Wide Brass	Narrow Brass	Aluminium	Stainless Steel
Primary Composition %	61 Cu	61 Cu	97.5 Al	58 Fe
Secondary Composition %	35 Zn	35 Zn	0.5 Mg	18 Cr / 10 Ni
Thermal Conductivity	115	115	150	14
Heat Flow Rate	0.368	0.24	0.26	0.201
Published Heat Flow Rate	0.36	0.28	0.28	0.17
Error	2.2%	-14%	-7.14%	15.7%

It is evident that cross sectional area of the sample does effect Heat flow rate between 12mm and 7mm Brass width samples (Table 1) (Equation 1). The narrow sample has 58% less cross sectional area, which transposes to a 24% reduction in heat flow rate, however both brass samples result in $\approx 2.2^\circ$ temperature difference equilibrium (Figure 4).

The initial peak of temperature difference arises due to the thermal conduction arising at the close thermistor which produces a large initial temperature difference (Pasco 2022). As time increases, the far thermistor receives more thermal energy and therefore finds an equilibrium point stated above (Figure 4).

Minimal error was observed between experimental and published data (Pasco 2022) (Table 1). The heat flow rates were higher in Narrow Brass and Aluminium and lower in Stainless Steel. This could be due to measurement differences and change in ambient temperature with the published data (Figure 4) (Pasco 2022).

3.2 Heat Pulse (*Following methods from section 2.2*)

Figure 5a, suggests the close thermistor at position T2 records temperature change more frequently with higher peaks and troughs experienced than at T1. The average time between close and far peaks is 9 seconds with an average temperature difference of 2.11° (Figure 5a) (Equation 2). This relationship is due to the aforementioned time required for the heat flow to pass through the sample.

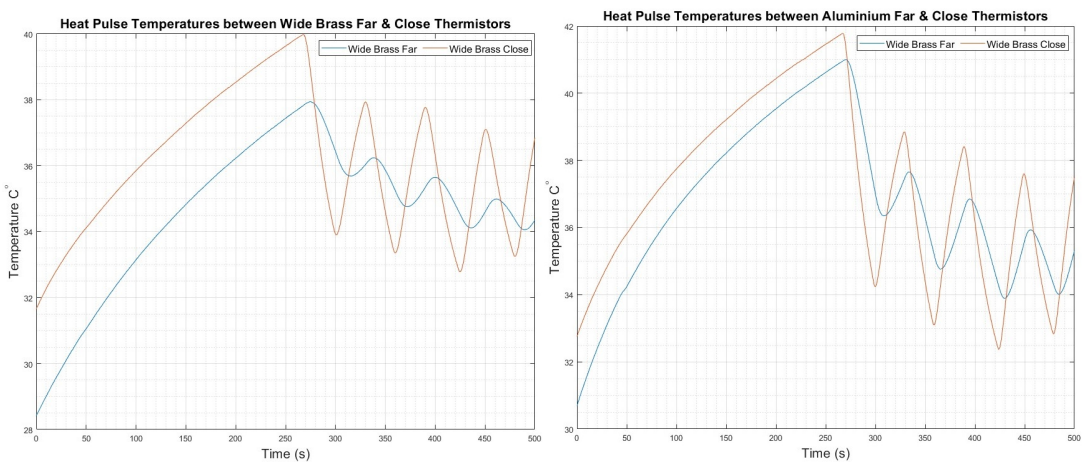


Figure 5: Wide Brass and Aluminium Temperatures during 30s cyclic heat pulse.

Figure 5b indicates the temperature changes due to the cyclic hot and cool functions in a similar manner as for wide brass. It is evident that Aluminium is a more efficient thermal conductor, due to the reduced vertical phase shift between each thermistor reading (Figure 5b). This concept is further reinforced as there was a greater amplitude change in the Aluminium sample during each cycle. The average time difference between aluminium thermal amplitudes is 6.5 seconds with a 1.48° average temperature difference (Figure 5).

This results in a 27% faster thermal conduction between thermistors with a 30% reduction in temperature difference between thermistors. Ozis and Tzou (1994) describes these changes in amplitude as the opposite flow of current, which cancels the positive and negative portions of the wave, resulting in a mean display. This is one wave however the direction of conduction is displayed as two (Ozis and Tzou 1994).

Thermal conductivity is a materials predisposition to conduct heat through the electron transport while heat flow rate is the amount and speed of heat energy at which the thermal conductivity occurs. Heat flow rate is effected by the surface area and distance the thermal energy travels (Cengel and Ghajar 2015). Hence why Wide Brass has a higher heat flow rate than Aluminium (Table 1). However the Aluminium conducts heat at a faster rate due to it's high thermal conductivity, which is a material property and is effected by temperature (Figure 4)(Cengel and Ghajar 2015).

3.3 Error and Recommendations

The primary recommendation would involve testing thermal conduction at different initial temperatures. It is a well known fact that thermal conductivity changes with a change in temperature. Liquid nitrogen can be used to reduce initial temperatures to -196°

It is also recommended for future studies to obtain different metals and alloys to broaden the array of tested materials. As Brass is a copper alloy, it would be interesting to measure thermal conductivity against pure copper.

4 Conclusion

In conclusion, the thermal conductivity properties and heat flow measurements have been verified with respect to the published data surrounding these specific metal alloys. It was hypothesized that materials with higher thermal conductivity values will have decreased time when measuring temperature change over a known distance. This relationship has been discovered in multiple experimental designs in both steady state conduction and oscillating steady state conduction.

As stated, Equation 1 indicates the relationship between thermal conductivity, temperature change and cross sectional area. The narrow brass sample resulted in a reduced heat flow, while maintaining the same thermal conductivity. It was seen that due to the alloy components of Stainless Steel, the inclusion of Chromium and Nickel reduces the available electrons for heat transfer compared to near pure Aluminium.

These results are concurrent with the literature in relation to thermal conduction and heat flow in the TD-8513 experimental protocol. This data will be used in engineering practice and material science to verify the current applications and understanding of thermal conductivity in metals.

References

1. Askeland, D.R., Fulay, P.P. and Wright, W.J. (2011). *The science and engineering of materials*. Stamford, Ct: Cengage Learning.
2. ASM Material Data Sheet. (2022) [online] Available at: <https://asm.matweb.com/search/SpecificMaterial.asp?bassnum=MA6063T5> [Accessed 29 May 2022].
3. AZoM (2019). Stainless Steels - Stainless 304 Properties, Fabrication and Applications. [online] AZoM.com. Available at: <https://www.azom.com/article.aspx?ArticleID=2867>.

4. Bluesea.com. (2019). Electrical Conductivity of Materials - Blue Sea Systems. [online] Available at: <https://www.bluesea.com/resources/108/Electrical%20Conductivity%20of%20Materials>.
5. Brass 360 Product Guide from Online Metals. (2022) [online] Available at: <https://www.onlinemetals.com/en/product-guide/alloy/360>.
6. Callister, W.D. (2018). Materials science and engineering : an introduction 10E. Hoboken, New Jersey: John Wiley Sons.
7. Chung, D.D.L. (2001). Materials for thermal conduction. Applied Thermal Engineering, [online] 21(16), pp.1593–1605. doi:10.1016/S1359-4311(01)00042-4.
8. Cengel, Y.A. and Ghajar, A.J. (2015). Heat and mass transfer : fundamentals applications. 5th Ed. New York McGraw-Hill Education Cop.
9. Engineering ToolBox (2019). Thermal Conductivity of Metals, Metallic Elements and Alloys. [online] Engineeringtoolbox.com. Available at: <https://www.engineeringtoolbox.com/thermal-conductivity-metals-d858.html>.
10. Ozis, M.N. and Tzou, D.Y. (1994). On the Wave Theory in Heat Conduction. Journal of Heat Transfer, 116(3), pp.526–535. doi:10.1115/1.2910903.
11. Pasco Heat Conduction Apparatus TD-8513. (2022). [online] Available at: <https://cdn.pasco.com/productdocument/Heat-Conduction-Apparatus-Manual-TD-8513.pdf> [Accessed 29 May 2022].

Appendix

Mathematical process was not included for Equation 1 and 2 due to the use of MATLAB 2022ra. Mathematical procedures can be acquired via contact of the author if required for experimental reproduction. However the values used for Equation 1 and 2 can be found in Table 1 and Figure 4. Robert Hawken, rch003@student.usc.edu.au

Variable flow rates of tube and plate heat exchanges in parallel and counterflow

Robert Hawken

School of Engineering, University of the Sunshine Coast.

1 Introduction

Heat exchangers are used in order to take advantage of the temperature gradient between hot and cold fluids without direct contact. Two common types of heat exchangers are the concentric tube (one pipe running parallel through a larger pipe) and the plate style (multiple layers of stacked plates). Both heat exchangers are fitted for either parallel or counter flow configurations (Cengel and Ghajar 2015).

A parallel heat exchanger is characterised by hot and cold fluids entering at the same orientation. Over a longer distance, the heat transfer rate in a parallel heat exchanger is most likely to become inefficient, unreliable and unpredictable in practice (Wetley, Rorrer & Foster 2020). The log mean temperature difference (L.M.T.D) is used to estimate the average temperature difference between fluids due to the decay style of a parallel system. A counterflowing arrangement involves cold fluid entering the system at the origin of the hot fluid. This ensures a predictable and somewhat linear relationship between temperature gradients as the effective length of heat exchange encompasses the full length of the system rather than the initial inlet (Kakac, Hongtan & Pramuanjaroenkij 2020).

It is primarily hypothesised that a counter flowing heat exchanger will have a higher L.M.T.D and overall heat transfer coefficient (U) over varying flow rates than a heat exchanger in parallel. Secondly, it is hypothesized that a plate heat exchanger will have a higher L.M.T.D and U value than a concentric tube heat exchanger.

1.1 Governing Equations

The coefficient of energy balance (C.E.B) is created by calculating the heat transfer absorbed by the system over the energy emitted by the system.

$$CEB = \frac{\dot{Q}_a}{\dot{Q}_e} \quad (1)$$

L.M.T.D is the natural logarithmic function with respect to the different water temperature recorded. For Parallel flow (Equation 2) and for Counter flow (Equation 3).

$$L.M.T.D = \frac{(TH_2 - TC_2) - (TH_1 - TC_1)}{\ln \left(\frac{TH_2 - TC_2}{TH_1 - TC_1} \right)} \quad (2)$$

$$L.M.T.D = \frac{(TH_1 - TC_2) - (TH_2 - TC_1)}{\ln \left(\frac{TH_1 - TC_2}{TH_2 - TC_1} \right)} \quad (3)$$

Overall heat transfer coefficient values were calculated by the heat transfer rate emitted over the mean heat transfer area by the L.M.T.D. (Appendix 1).

$$U = \frac{\dot{Q}_e}{A \cdot L.M.T.D} \quad (4)$$

2 Experimental Design

2.1 Concentric Tube heat exchanger

In the parallel flow configuration, a TD360a heat exchanger with 60° hot water flow of 3 L/min was applied with variable cold water intake of 3 L/min, 2 L/min, 1 L/min and 0.5 L/min (Figure 1). Intake, central and exit temperatures were recorded for each flow rate after five minutes of equilibrium time.

This experimental design was repeated with the cold water intake reversed into a counter flow arrangement (Figure 1).

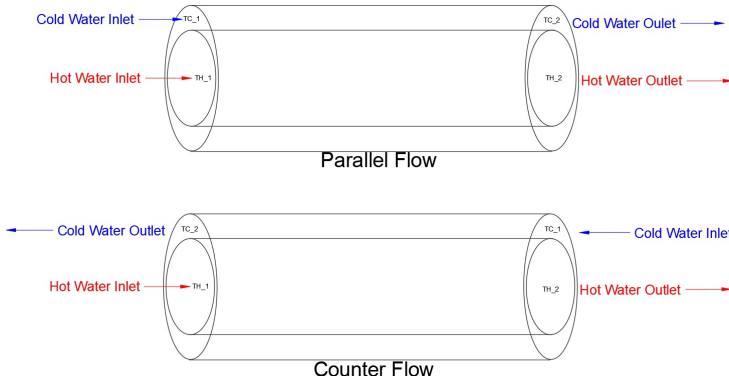


Figure. 1: Water flow directions for Parallel and Counterflow Concentric Tube Arrangements.

2.2 Plate heat exchanger

After each flow rate was tested, a TD360b plate heat exchanger was installed and both parallel and counterflow variable cold flow rates were repeated with 3 minute equilibrium time (Figure 2).

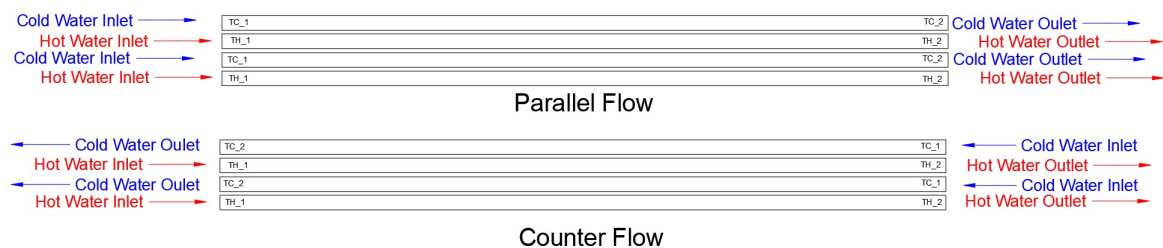


Figure. 2: Water flow directions for Parallel and Counterflow Plate Arrangements

2.3 Numerical Analysis

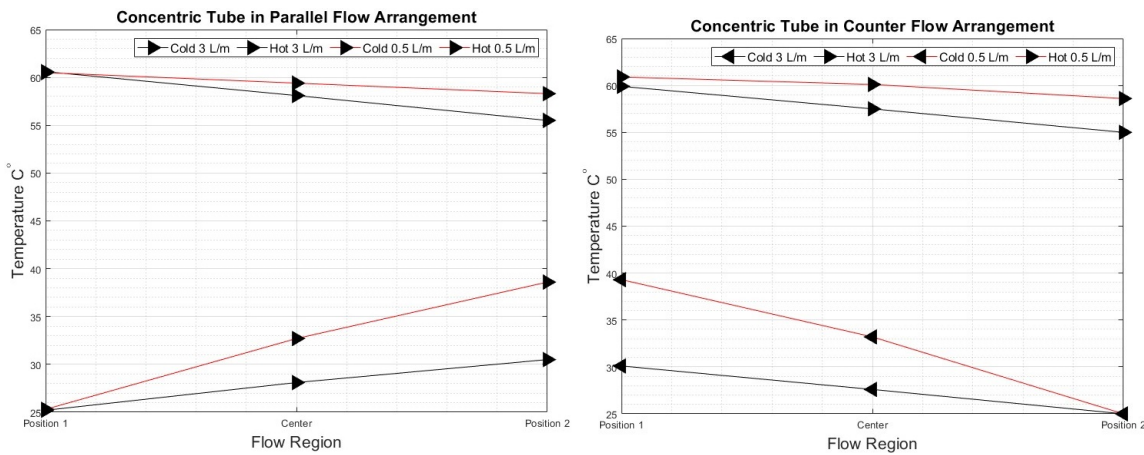
Graphical illustrations were completed using MATLAB 2022Ra edition and line diagrams with AutoCAD 2023. TD360a/b Bench top heat exchanger by TecQquipment (2018) included the relevant formulae used for the Governing equations in section 1.1. Density, specific heat capacity, heat transfer rate and temperature efficiency calculations were completed via Microsoft Excel 365 (Appendix 1).

3 Results and Discussion

3.1 Concentric Tube In Parallel and Counter Flow Arrangement

Temperature recordings for concentric tube in parallel flow arrangement is displayed across all four cold flow rates at Position 1 (inlet) and Position 2 (outlet)(Figure 3a). The 0.5 L/min flow rates resulted in the largest temperature increase of cold water reaching $\approx 40^\circ$ at both outlet instances (Position 2). This suggests the slower flow rate acts more like a condenser with a larger change in cold water temperature than hot water (Wetley et.al. 2020).

Conversely the temperature difference of the 3 L/min flow rates remained steady, suggesting the increased flow rate, reduced heat transfer (Figure 3a). Figure 3b displays concentric tube in the counter flow arrangement. In support of the trends outlined above, 0.5 L/min flow rate experienced the highest temperature difference in counter flow arrangement as seen in (Naphon 2006). However there was no significant temperature difference between flow directions at the same flow rate (Figure 3b). Parallel flows can cause a higher thermal stress in materials due to the large temperature difference at the inlet (Position 1) (Thulukkanam, 2013).



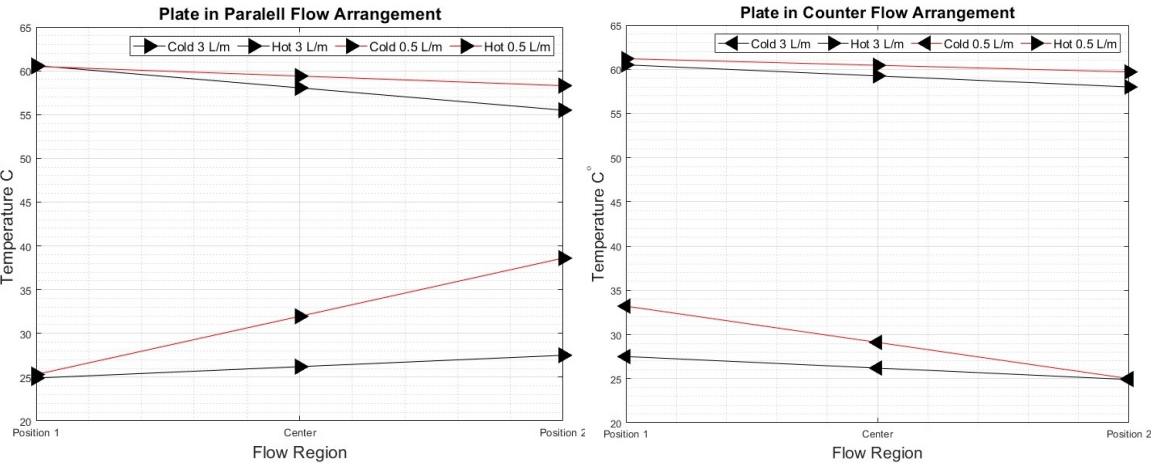
(a) Concentric Tube Parallel Flow

Figure. 3: Inlet and outlet temperature of concentric tube heat exchanger in parallel and counter flow arrangements.

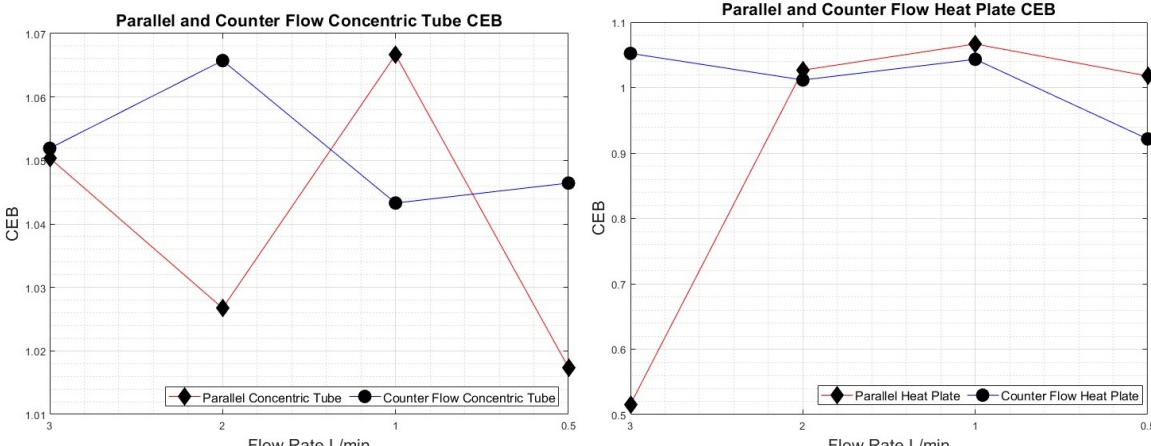
3.2 Heat Plate in Parallel and Counter Flow Arrangement

The inlet, average and outlet temperature recordings for the heat plate in the parallel and counter flow arrangement are displayed across all four cold flow rates in Figure 4 (a&b). In line with section 3.1, it is seen that the 0.5 L/min flow rates resulted in the largest temperature increase of cold water ($\approx 13^\circ$ parallel & $\approx 8^\circ$ counterflow) compared to the 3 L/min flow rate ($\approx 2.5^\circ$ parallel & counterflow).

As stated, a greater cold and hot water temperature change occurred in parallel flow rather than the counter flow arrangement (Figure 4b). This is contrary to the stated hypothesis and current literature. Thulukkanam (2013) states that a counterflow system is the most efficient single pass system at the same flow rates and temperatures. Due to the nature of parallel and counter flow inlet temperature difference, it is more appropriate to use L.M.T.D (as both inlet and outlet temperatures are known) and U values outlined in Table 1 (Thulukkanam 2013).



The coefficient of energy balance (C.E.B) for the heat plate in the parallel and counter flow arrangement is displayed across all four cold flow rates (Figure 5a & b). It is seen that the parallel direction in both heat exchangers has a higher variance in coefficients $\approx 0.5 - 1.05$. This indicates an unsteady relationship between energy absorbed and emitted. In both heat exchangers, the counter flow direction shows a steady heat exchange between heat emitted and absorbed ≈ 1.05 . Further calculations of L.M.T.D and U are needed for final conclusions (Thulukkanam, 2013).



3.3 Analysis of L.M.T.D and Overall Heat transfer coefficient

Table 1 refers to the L.M.T.D values for the concentric tube and plate heat exchanger across both flow directions at 3 L/min and 0.5 L/min. It is evident that there is no significant difference ($\approx 1\%$) between the L.M.T.D values in the concentric tube between Parallel and Counter flow operations at either 3 L min or 0.5 L min.

However in the plate system, there is a significant temperature difference in regards to 3 L/min ($\approx 4\%$) and counter flow ($\approx 17\%$), both in favour of counter flow. This indicates the highest L.M.T.D value is the counter flow plate at 3 L/min (33.05) and the lowest in parallel plate (26.7°. This is supportive of the current implementation of heat exchangers in applications (Cengel and Ghajar 2015).

As heat exchangers are considered steady state devices, it is more suitable to use a counterflow system, due to the stable L.T.M.D profiles for engineering design (Kakac et. al. 2020)

Table 1 also indicates that the highest L.M.T.D occurred at a flow rate of 3 L/min as more fluid is available for heat transfer than at 0.5 L/min (Cengel and Ghajar 2015).

Table 1: L.M.T.D (°C) Tube and Plate Heat Exchanger with Variable Flow rates

Cold Flow	Parallel Tube	Counter Tube	% Δ	Parallel Plate	Counter Plate	% Δ
3 (L/min)	29.89	29.90	-0.002	31.69	33.05	4.277
0.5 (L/min)	26.70	27.16	1.70	26.70	31.23	16.95

At 3 L/min, parallel tube was more efficient $\approx 4\%$ and counter flow was $\approx 3\%$ more efficient at 0.5 L/min, however both are not significantly different (Table 2). There was a 112% and 70% difference between efficiency in favor of the parallel configuration over the counterflow in a plate heat exchanger. This is contrary to the current research and expectations of findings. It is expected that a plate heat exchanger would have a higher U value, due to, two cold flows surrounding each hot flow (Cengel and Ghajar 2015). It is also expected that counter flow arrangements have a higher L.M.T.D, due to the consistent temperature gradient profile patterns outlined in section 3.1 (Hesselgreaves, Law & Reay 2016).

Table 2: $U \left(\frac{W}{M^2 \cdot K} \right)$ Tube and Plate Heat Exchanger with Variable Flow rates

Cold Flow	Parallel Tube	Counter Tube	% Δ	Parallel Plate	Counter Plate	% Δ
3 (L/min)	1756.32	1687.80	4.06	1656.88	778.51	112.82
0.5 (L/min)	847.83	871.27	-2.69	847.83	494.08	71.59

3.4 Errors and Recommendations for Variable Flow Rate

The primary errors in this experiment is that TC_1 should always be below 20° at every instance, which was not adhered to. The second major error was a 5 minute equilibrium time for the concentric tube and 3 minutes for the plate heat exchanger rather 5 minutes for both. As it was not possible to measure the temperature in the centre of the plate exchanger, the average was used between inlet and outlet.

Appendix 1 indicates that the centre temperature was not always the average for the concentric tube arrangement and could influence the plate results. When

"no significant difference" was determined between heat exchangers, the plate heat exchanger results could become significantly different if both tests were measured at 5 minute equilibrium times. However due to the nature of exponential temperature change, it was deemed unsuitable for exponential extrapolation to estimate plate heat exchanger data at 5 minutes (Appendix 2).

4 Conclusion

As seen there are numerous expected and unexpected outcomes from this experimental design, further recommendations will be considered before replication and systemic review of results from other TD 360 results. Due to the vast array of variables, the conclusion will be outlined in separate points per variable.

4.1 Variable Flow rates

1. 0.5 L/min flow rates had the highest increase in outlet cold water temperature for the concentric tube compared to 3 L/min.
2. 3 L/min flow rates had the highest decrease in outlet hot water temperature for the concentric tube compared to 0.5 L/min.
3. The same trends of flow rates of 1 & 2 were seen in the plate heat exchanger.
4. This indicates that a 0.5 L/min flow rate should be used if that aim is to heat up cold water and 3.0 L/min should be used if the aim is to decrease the temperature of hot water for either heat exchanger.

4.2 Parallel or Counter flow orientation

1. There was no significant difference in both outlet temperatures of the same flow rate between either flow direction in the concentric tube heat exchanger.
2. There was a significant difference in cold water outlet temperatures, with the largest difference in the parallel flow direction for the plate heat exchanger.

4.3 Conclusion of L.M.T.D

1. There was no significant difference between L.M.T.D values at the same flow rate in the concentric tube.
2. There was a significant difference between L.M.T.D values at the same flow rates in the plate heat exchanger.
3. The highest L.M.T.D values occurred in the counter flow arrangement as expected however the largest mean difference was at 3 L/min.

4.4 Conclusion of Heat transfer rate

1. There was no significant difference between thermal transfer rate in concentric tube heat exchanger at the same flow rate.
2. There was a significant difference between thermal transfer rate in plate heat exchanger with the parallel configuration the preferred option.

References

1. Abu-Khader, M.M. (2012). Plate heat exchangers: Recent advances. Renewable and Sustainable Energy Reviews, [online] 16(4), pp.1883–1891. doi:10.1016/j.rser.2012.01.009.
2. Hesselgreaves, J.E., Law, R. and Reay, D. (2016). Compact Heat Exchangers : Selection, Design and Operation. [online] Elsevier Science. Available at: <https://www.elsevier.com/books/compact-heat-exchangers/hesselgreaves/978-0-08-100305-3> [Accessed 26 Nov. 2019].
3. Thulukkanam. K (2013). Heat Exchanger Design Handbook, Second Edition. Crc Press.
4. Naphon, P. (2006). Second law analysis on the heat transfer of the horizontal concentric tube heat exchanger. International Communications in Heat and Mass Transfer, 33(8), pp.1029–1041. doi:10.1016/j.icheatmasstransfer.2006.05.001.
5. S Kakac, Hongtan Liu and A Pramanjaroenkij (2020). Heat exchangers : selection, rating, and thermal design. Boca Raton, Fl: Crc Press.
6. TecQuipment. (2018). Heat Exchanger Service Module. [online] Available at: <https://www.tecquipment.com/heat-exchanger-service-module>.
7. Welty, J. Rorrer. G, and Foster. D (2020). Fundamentals Of Momentum, Heat, And Mass Transfer. 6th Ed. S.L.: John Wiley.